Tissue Eng Regen Med (2018) 15(2):231–247
https://doi.org/10.1007/s13770-017-0106-6

Online ISSN 2212-5469
Print ISSN 1738-2696

ORIGINAL ARTICLE

Osteogenic Nanofibrous Coated Titanium Implant Results in Enhanced Osseointegration: *In Vivo* Preliminary Study in a Rabbit Model

Siddhartha Das[1,2] · Sandeep Gurav[3] · Vivek Soni[1] · Arvind Ingle[4] · Bhabani S. Mohanty[4] · Pradip Chaudhari[4] · Kiran Bendale[4] · Kanchan Dholam[3] · Jayesh R. Bellare[2,5]

Received: 30 August 2017 / Revised: 21 November 2017 / Accepted: 28 November 2017 / Published online: 19 January 2018

Abstract A titanium implant surface when coated with biodegradable, highly porous, osteogenic nanofibrous coating has shown enhanced intrinsic osteoinductive and osteoconductive properties. This coating mimics extracellular matrix resulting in differentiation of stem cells present in the peri-implant niche to osteoblast and hence results in enhanced osseointegration of the implant. The osteogenic nanofibrous coating (ONFC) consists of poly-caprolactone, gelatin, nano-sized hydroxyapatite, dexamethasone, ascorbic acid and beta-glycerophosphate. ONFC exhibits optimum mechanical properties to support mesenchymal stem cells and steer their osteogenic differentiation. ONFC was subjected to various characterization tests like scanning electron microscopy, Fourier-transform infrared spectroscopy, x-ray diffractometry, thermal degradation, biomineralization, mechanical properties, wettability and proliferation assay. In pre-clinical animal trials, the coated implant showed enhanced new bone formation when placed in the tibia of rabbit. This novel approach toward implant bone integration holds significant promise for its easy and economical coating thus marking the beginning of new era of electrospun osteogenic nanofibrous coated bone implants.

Keywords Osteogenic nanofibrous coating · Osseointegration · Titanium implant

1 Introduction

The uses of implants especially oral implants have increased several folds due to its massive clinical success world-wide. This may be attributed to the fact that oral implants undergoes interference fitting with the bone and thus have remarkable capability of restoring the form and function of masticatory apparatus irrespective of any pathology of the stomatognathic system [1]. Branemark et al. [2] first reported the process of bone integration with titanium implants, and later called this process as "osseointegration". The titanium implant interact with biofluid, protein and cells upon its insertion in the jaw [3] followed by blood clot giving rise to angiogenesis, osteo-proginator cell migration etc. [4]. Briefly, there are two types of responses upon placement of implants; fibrous capsule formation [5, 6] and bone integration i.e. direct implant-bone contact without an intervening connective tissue (osseointegration) [2]. Osseointegration is desirable

Electronic supplementary material The online version of this article (https://doi.org/10.1007/s13770-017-0106-6) contains supplementary material, which is available to authorized users.

✉ Jayesh R. Bellare
jb@iitb.ac.in

1 Department of Biosciences and Bioengineering, Indian Institute of Technology Bombay, Mumbai 400076, India

2 Department of Chemical Engineering, Indian Institute of Technology Bombay, Mumbai 400076, India

3 Tata Memorial Centre, HBNI, Mumbai 400012, India

4 Advanced Centre for Treatment, Research and Education in Cancer, Navi Mumbai 410210, India

5 Wadhwani Research Centre for Bioengineering, Indian Institute of Technology Bombay, Mumbai 400076, India

while fibrous tissue capsule formation around the dental implant leads to clinical failure [1]. Moreover, biomechanical factors and patient's oral hygiene also contribute to the long-term success of the implants [7, 8]. The amount and nature of osseointegration in titanium implants are determined by surface topography which includes surface roughness [9], wettability [10, 11], and surface morphology [12, 13]. Over the years, implants manufacturer have developed wide variety of surfaces with different surface topography exhibiting range of roughness, however it remains a matter of debate regarding the precise modification of specific parameter for which the implant would display optimal dynamics of osseointegration.

To obtain an optimal bone implant surface, the implant should preferably present an osteoinductive and osteoconductive surface irrespective of site of implantation, and regardless of quality or quantity of bone [14].The approaches for modification of implant surface could be physicochemical, morphological or biochemical [15]. Physicochemical method employs modification of surface charge, surface energy or composition on titanium implants to obtain a favourable biological responses but it shows to lack specificity [16, 17]. By far, the most valued topic among dental implant design alterations are modification of surface morphology which includes the modification of surface properties like surface roughness, wettability etc. to get desirable cellular and tissue responses [12]. Hence, a wide variety of dental implants are being fabricated. Depending on surface topography implants are classified as concave, convex or planar implants [18–20]; direction/orientation of irregularities—isotropic and anisotropic implants [21] and extent of roughness-smooth (< 0.5 μm), minimally rough (0.5–1 μm) moderately rough (1–2 μm) and rough (> 2 μm) implants [21]. Machined or turned dental implants are the first generation dental implants with smooth surface but literature suggests that it cannot be used in the compromised bony region apart from exhibiting poor osseointegration [22]. Titanium implants were also subjected to chemical etching by strong acids like hydrofluoric (HF), nitric (HNO_3), and sulphuric acid (H_2SO_4) or a combination of these to get a homogeneous roughness however sometimes they lead to porosities ranging from 0.5 to 2 μm [23], further the suitability of these acids in etching are not determined and warranted further tests [24]. Plasma spray involves depositing thick layers of hydroxyapatite or titanium on the implant surface resulting in increased surface roughness and surface area but some reports claim that such implants have less interfacial bond strength [25]. Grit blasting employs sand, hydroxyapatite, alumina, or TiO_2 particles that are projected onto the implant surface for roughness but the surface produced is prone to bacterial contamination [26]. Biochemical method includes incorporation of biologically active molecules like bisphosphonates into the surface of the titanium implants, however it does not follow a linear releasing pattern [27] apart from inducing gastric injury and delayed ulcer healing in rodents [28]. Although several coated implants are known and reported, they suffer from limitation as discussed above. Therefore, there is a need and scope for coated endosseous implants, especially coated endosseous root form dental implants that address the problems in the existing prior art and exhibit improved or accelerated osseointegration.

Moreover, further to the discussion, the extracellular matrix (ECM) is an ultra-structural three-dimensional complex mixture of functional proteins, glycoproteins, and proteoglycans occupying the intercellular space of all tissues including alveolar bone [29]. ECM are involved in number of functions like structural support and tensile strength, providing focal adhesion sites for cell surface receptors, cell signalling etc. [30]. They are vital and are known to be in a state of dynamic equilibrium with its surrounding microenvironment. Reports suggest that ECM provides niche to stem cells and thereby shields these cells from various stimuli like apoptosis and differentiation. However, they must periodically activate themselves to produce progenitor cells to strike a balance between dormancy and active state [31].

In addition, the artificial biodegradable nanofibres produced by electrospinning process mimics these ECM and are known to induce certain tuneable favourable features like cell–biomaterial interactions, shaping cell morphology, guiding cell migration, gene expression and differentiation etc. [32]. Artificial ultrafine nanofibrous scaffold mimicking ECM could be fabricated by electrospinning process [33]. The 3D porous scaffold leads to enhance tissue neogenesis by virtue of its high surface area, porosity and biodegradability [34]. Notably, biocompatible polymers like polycaprolactone have shown comparable features to that of collagen in ECM [35]. Gelatin, a natural biopolymer is added to enhance the bioactive functions like favourable cell–coating interactions etc. [35]. Further, there are numerous reports in the literature describing the osteoinductive potentials of dexamethasone, ascorbic acid and beta-glycerophosphate [36]. Earlier, it was reported that dexamethasone induced mesenchymal stem cell differentiation into osteoblast is mediated by LIM-domain protein further by activating WNT/β-catenin signaling-dependent Runx 2 expression [37]. Another possible mechanism could be the modulation of Runx 2 phosphorylation via the mitogen-activated protein kinase phosphatase [38]. Ascorbic acid performs vital role in production of Col 1 into the ECM resulting in increased binding of α1β1 integrins which are known to be prerequisite for osteogenic differentiation [36, 39]. B-Glycerophosphate aids in phosphorylation of ERK1/2 and acts as a source of phosphate

for hydroxyapatite [36]. Additionally, hydroxyapatite, an osteoconductive agent, acts as a local source of calcium and phosphates that are vital for mineralization of surrounding tissues [40–45]. Hence, for the preliminary *in vivo* evaluation, we chose a dual optimization strategy by incorporating both osteoinductive and osteoconductive chemicals in deriving the ECM mimicking osteogenic nanofibrous coating.

We hypothesize that titanium implants coated with our novel osteogenic nanofibres will enhance the rate of osseointegration (Fig. 1A). Herein, we were successful in fabricating the nanofibrous coating having osteogenic property around the titanium implant by modifying the electrospinning set-up (Fig. 1B) and conducted its characterization study. The aim of the study was to evaluate the biological properties of the osteogenic nanofibres coated (ONFC) titanium implant *in vivo*.

2 Materials and methods

2.1 Materials

Polycaprolactone, Type A-Gelatin, and Resazurin sodium salt were purchased from Sigma Aldrich, USA. 2,2,2-Trifluoroethanol was obtained from Spectrochem, India. Titanium bone screws, 2 mm × 5 mm were purchased from Lynx, Equinox, Netherlands. Beta-glycerophosphate, Dexamethasone, Ascorbic acid, Hank's balanced salt solution, Fetal bovine serum, Amphotericin B, trypsin-EDTA solution were purchased from Himedia. Hydroxyapatite was obtained from Budenheim, Germany.

2.2 Fabrication of nanofibrous coating around the titanium implant

Polycaprolactone 5% (w/v), gelatin type A 0.5% (w/v), dexamethasone 0.032% (w/v), Beta-glycerophosphate 0.5% (w/v), ascorbic acid 0.04% (w/v), and hydroxyapatite 0.04% (w/v), were dissolved in 2,2,2-trifluoroethanol to get a uniform polymer blend.

The polymer solution was aspirated into the syringe and placed in the syringe pump. A minimal flow rate of 0.34 ml h^{-1} was maintained. The distance between the tip of the needle and collecting plate was approximately 13 cm. The electric field induced by DC voltage results in changing the tear shaped drop coming out of the needle into an elongated conical structure known as tailor cone which burst into nanofibres. Voltage difference applied was kept preferably at 15 kV. A DC motor attached to power source was used to coat the titanium bone screws. The tip of each titanium screw was attached to the extended shaft of the DC motor via chuck and later placed between the tip

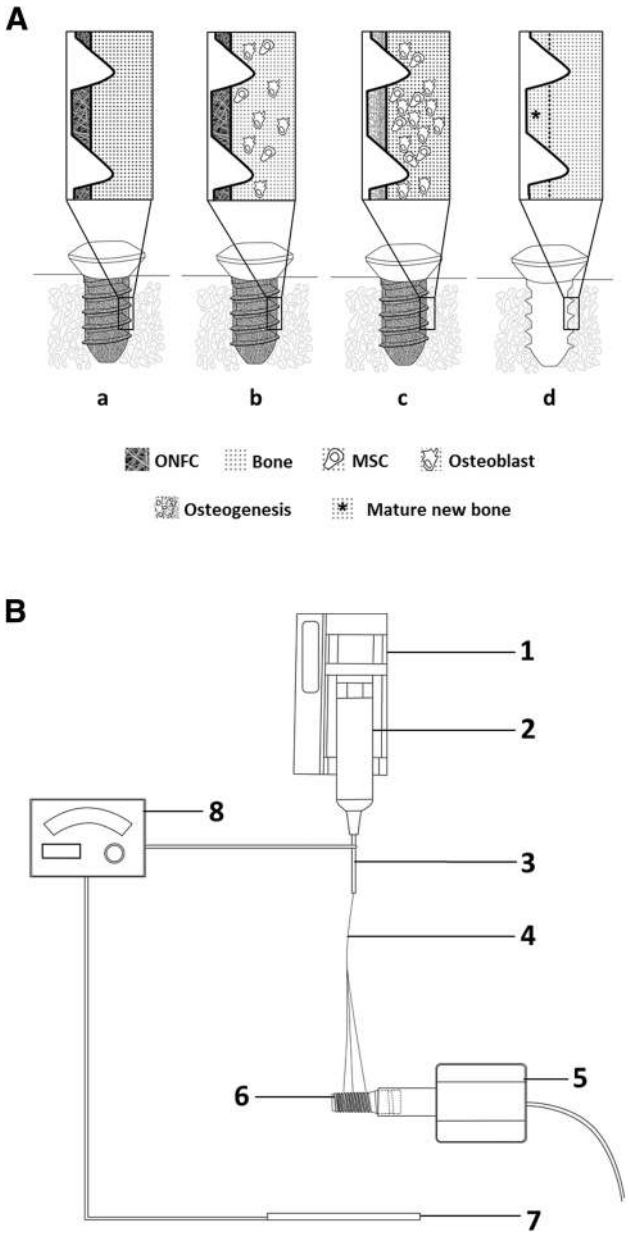

Fig. 1 Mechanism for enhanced osseointegration in ONFC implants and schematic for coating osteogenic nanofibres around the titanium implants. **A** (a) ONFC titanium implant is placed aseptically in the bone, (b) ONFC implant provides favourable niche for osteoblasts and undifferentiated mesenchymal stem cells in the peri-implant zone to attach, grow and proliferate, (c) cells lodge in the ONFC which mimics extracellular matrix and starts the process of osteoinduction and osteoconduction, (d) new bone formation (mesial to the dotted line) results in enhanced osseointegration of the implant. **B** Electrospinning apparatus for coating osteogenic nanofibres around the implants: 1—syringe pump, 2—syringe, 3—needle, 4—nanofibres, 5—DC motor, 6—titanium bone screws attached to the shaft of the motor, 7—collector plate, 8—voltage generator

of the needle and the copper collecting plate covered with aluminium foil. The distance of the screw from the tip of the needle was ∼ 6 cm. The nanofibres were allowed to

coil around the rotating screws attached to the shaft of motor for 2 min. Rate of rotation of shaft was 50 rpm (Fig. 1B).

2.3 Characterization of nanofibrous coating

2.3.1 Environmental scanning electron microscopy (ESEM)

The electrospun osteogenic nanofibrous coated (ONFC) and uncoated titanium bone screws were analysed using an FEI Quanta 200, operating under high-vacuum conditions at an accelerating voltage of 0.7–30 kV. All samples were sputter coated with platinum using auto fine coater JFC-1600 (JEOL, Japan), utilizing 10 mA current for 250 s prior to imaging. The fibrous coating was characterized by fibre distribution, uniformity and general topography.

2.3.2 Fourier transform infrared (FTIR) spectral analysis

ATR-IR spectrometer, Bruker Tensor 27 (Germany) was used to scan the osteogenic nanofibrous coatings (ONFC) and its individual additives viz. polycaprolactone, gelatin, beta-glycerophosphate, dexamethasone, ascorbic acid and hydroxyapatite for comparative study. The samples were dissolved in chloroform and placed between the CsBr plates and loaded onto the instrument for spectral analysis. FTIR spectra were recorded from 4000 to 500 cm^{-1} with a resolution of 1 cm^{-1}.

2.3.3 X-ray diffraction (XRD) analysis

XRD patterns were recorded by X-ray diffractometer (SmartLab, X-ray diffractometer, Rigaku) using Cu anode at 40 kV and 30 mA in 2θ range of 10°–90°. Samples consisting of osteogenic nanofibres (ONFC) and its individual additives were loaded in the instrument.

2.3.4 Thermogravimetric (TGA) analysis

The examination of thermal properties of osteogenic nanofibrous coating (ONFC) and its individual additives were performed by Thermo gravimetric differential thermal analyser (Model-Diamond TG/DTA) Perkin Elmer, USA. Approximately, 3 mg of samples were used per run. Samples were heated from room temperature to 1000 °C in a N_2 environment at a heating rate of 10 °C min^{-1}.

2.3.5 Mechanical properties

The ONFC and PCL nanofibres were evaluated for their mechanical properties by using a Universal Testing Machine (Tinius Olsen, USA). The samples (n = 7) for each group were cut into 10 mm width and 32 mm in length. The ends of the samples were mounted on the gripping units of the machine, and a load of 10 kN at an extension rate of 10 mm min^{-1} was applied until failure.

2.3.6 Surface area and porosity analysis

Nitrogen adsorption isotherms at 77 K were measured by using a surface area analyser (Quantachrome Autosorb As-1 Version-1.55). The pore size distribution (PSD) was calculated from the adsorption branch using the Barrett–Joyner–Halenda (BJH) method. Both ONFC and PCL nanofibrous coatings were subjected to the comparative analysis.

2.3.7 Atomic force microscopy analysis

The surface morphology of the osteogenic nanofibres were analysed using the atomic force microscope (AFM) in tapping mode (MPF-3D-BIO, Asylum Research, Oxford instruments) using a 100 kHz silicon nitride tip (Olympus) under ambient conditions with scanned areas of 20 μm × 20 μm. The images were scanned at pre-determined areas for each sample. The surface topography of osteogenic nanofibrous coating (ONFC) and pure titanium bone screws were compared and analysed.

2.3.8 Contact angle measurement

Water contact angles were obtained using the sessile drop technique with a GBX scientific instrument (Romans, France). The drop image was stored by a video camera (Nikon) and an image analysis system (WinDrop++) calculated the contact angle from the shape of the drop. Both the samples i.e. ONFC and PCL nanofibres (n = 7), were kept on a sample stage and 1.5 μL of distilled water was dropped at pre-determined sites with time period (T = 100 s) observation. The average of left and right angles for each drop was used for calculation of the final contact angle. All wetting angle experiments were conducted in a laboratory atmosphere controlled at 23 °C with 70% relative humidity. The wettability of pure titanium implant was obtained from literature [46–48].

2.3.9 Cell viability assay

The viability and proliferation of L949 mouse fibroblast (3.5×10^6 cells) seeded in ONFC and PCL nanofibrous coating were investigated by Resazurin sodium salt. After 48 h of incubation at 37 °C in 5% CO_2, complete media having resazurin dye at concentration of 200 μM were added in the respective wells. Measurements of the reduced resazurin to resorufin were conducted by using SpectraMax

M2 microplate reader (molecular devices) at the excitation wave length of 560 nm and the emission wave length of 590 nm.

2.3.10 Biomineralization activity

Equal weight and shape of ONFC and PCL nanofibres were immersed in 5 ml of simulated body fluid (SBF) for a period of 7, 14 and 21 days at 37 °C. SBF was prepared as described previously by Kokubo et al. [49]. Later, these nanofibrous mats were rinsed with distilled water and allowed to dry at room temperature. The mineralization response of the ONFC and PCL nanofibres were evaluated by environmental scanning electron microscopy (ESEM) and energy-dispersive x-ray spectroscopy (EDX).

2.4 *In vivo* study

2.4.1 Animal surgery

One skeletally mature male New Zealand white rabbit, weighing more than 3 kg was used in the study. The experiment was approved by the local ethical committee for animal experiments, ACTREC-TMC Navi Mumbai—WIHC/3596—TMH-IITB-ACTREC (Animal study proposal no. 03/2016). The rabbit was screened for pathological infections and was found healthy with normal blood biochemistry and haemogram. The pilot rabbit received two screw type titanium implants in each tibia. Before the surgery, ONFC and uncoated titanium implant were sterilized by irradiating with 25 kGy of gamma rays for 36 h. On the day of surgery, the rabbit was anesthetized with intramuscular injection of 35 mg kg^{-1} body weight of ketamine and 5 mg kg^{-1} body weight of xylazine. The surgical sites i.e. medial part of tibia, were prepared by clipping the fur on both hind limbs from the ankles to above the knees. The surgical area was aseptically cleaned with chlorhexidine solution followed by disinfection with 10% povidone iodine and 70% alcohol. A sterile bandage was wrapped around both the feet of rabbit and later tied and fixed with the operating table to avoid sudden jerking of limbs during the surgical procedure and subsequently draped for surgery. The skin above the proximal tibia was incised and the subcutaneous tissue was bluntly dissected all the way down to the periosteum. Periosteum was incised and bone was exposed. Implant sites (two), one in the proximal diaphysis and one in the central diaphysis, at a distance of 3 cm in between, were prepared in each tibia. Cavities of 6 mm depth reaching into the medulla were created by intermittent drilling with a 2 mm drill bit under continuous irrigation with normal saline. The ONFC and control implant (two of each) were inserted into the prepared sites on the left and right tibia respectively (see supplementary data).

Subcutaneous tissues were sutured using absorbable 2-0 chromic catgut and skin was closed using 2-0 non absorbable silk suture. Povidone iodine 5% ointment was applied on the stitches and later 0.03 mg kg^{-1} buprenorphine was administered subcutaneously. The rabbit was placed in a cage during recovery. Postoperative radiographs (AP and mediolateral) was taken immediately after surgery to rule out intraoperative fractures and complications and to help determine implant orientation and alignment (see supplementary data). Post-operative pain control was achieved with subcutaneous administration of 0.05 mg kg^{-1} buprenorphine. After 6 weeks, post-surgery, the rabbit was euthanized with Pentobarbital 100 mg ml^{-1}.

2.4.2 Micro CT analysis

The tibia of rabbit (n = 2) containing ONFC and control implants were scanned by a micro-computed tomography (Gamma Medica-Ideas, FLEX^{TM} Triumph^{TM} Pre-Clinical Imaging System) in an axial, sagittal and coronal direction, being horizontal for axial/sagittal and vertical for coronal to the long axis of the implant to compare the bone mineral density (BMD) and bone mineral content (BMC) of peri-implant area. The samples were scanned at 40 keV voltage, with exposure time of 600 ms. The focal spot was 84 μm with 2× magnification having field of view (FOV) 59.2 mm. The acquisition time was 19 min. The data was observed and analysed by MicroView and OsiriX software respectively.

2.4.3 Histology

Histological analysis of peri-implant tissue for ONFC and uncoated titanium implant were analysed. The tissues samples were fixed with 10% neutral buffered formalin, sectioned, dehydrated with graded series of ethanol, defatted in acetone, perfused with resin, polished and stained with Stevenel's blue. An optical microscope was used to examine the stained bone–implant interface for evaluation of regenerated osseous tissue.

2.4.4 Statistics

The statistical significance of the results were evaluated using the paired Student's t test. Null hypothesis was rejected at $p < 0.05$. Data significance is indicated with (*) for $p < 0.05$ (**) $p < 0.01$ and (***) $p < 0.001$. Results are reported as mean ± SEM (standard error of mean).

3 Results and discussion

3.1 Characterization study of nanofibrous coating

The surface appearance of the mechanically polished pure Ti sample (uncoated) represented the distinct orientation of irregularities (anisotropic) exhibiting tiny fissures and fuzzy grain edges with smooth shapes formed by virtue of its manufacturing process (Fig. 2B). Following electrospinning, the nanofibrous coating was examined under scanning electron microscopy. The individual fibres of the nanofibrous coating had an average diameter of 224 ± 5 nm. SEM images revealed that the fibres were randomly oriented and were bead free having mostly uniform diameter (Fig. 2D). It is to be noted that the individual fibres exhibited somewhat a flatter rather than a circular morphology in cross section mostly due to evaporation of the trapped solvent leading to collapsing of the fibres [50, 51].

In the Fig. 3A, PCL, PCL-G and ONFC exhibits infrared spectra in the same region suggesting that they have same chemical bond. Some of the peaks that were common to ONFC, PCL and PCL-G are 2945 cm^{-1} due to CH_2 stretching, (falls in the first region and have range from 4000 to 2500 cm^{-1} corresponds to N–H, C–H and O–H bond) 2866 cm^{-1} due to CH_2 stretching, (falls in the first region and have range from 4000 to 2500 cm^{-1} corresponds to N–H, C–H and O–H bond) 1730 cm^{-1} due to carbonyl stretching, (falls in the third region and have range from 2000 to 1500 cm^{-1} corresponds to absorption caused by double bond such as C=O, C=N and C=C) 1242 cm^{-1} due to COC stretching, (falls in the fourth region and have range from 1500 to 400 cm^{-1}) [52, 53]. The IR band of the amide group (NH_2) could be seen in the spectrum of ONFC and PCLG due to incorporation of

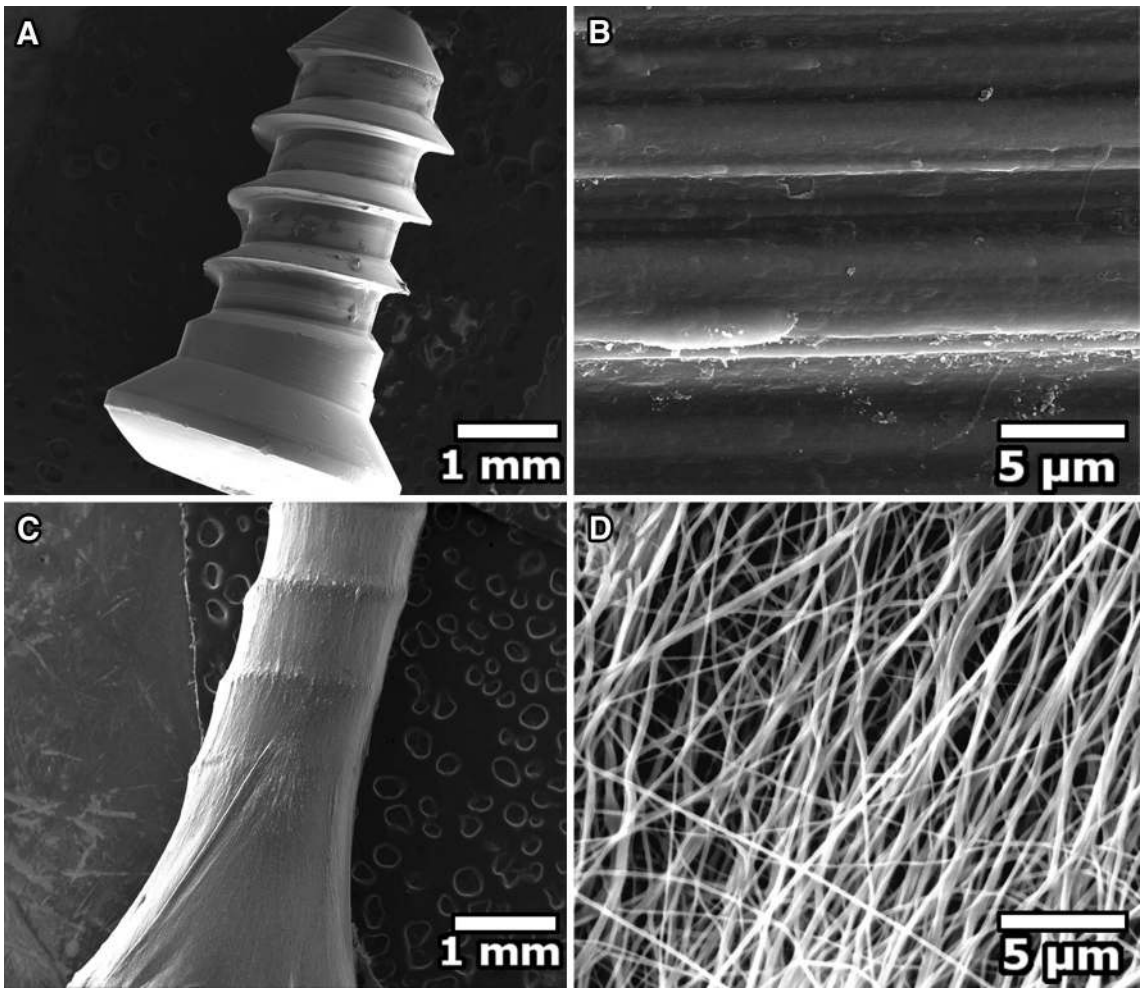

Fig. 2 Scanning electron microscope photographs of uncoated and coated titanium implant. **A** Uncoated titanium implant (×50 magnification), **B** uncoated titanium implant (×12,000 magnification), **C** coated titanium implant (×50 magnification), **D** coated titanium implant (×12,000 magnification). Smooth and uniform osteogenic nanofibrous coating around the titanium implant was observed when the applied solution voltage, feed rate and the tip-to-collector distance were 15 kV, 0.34 ml h^{-1} and 13 cm respectively

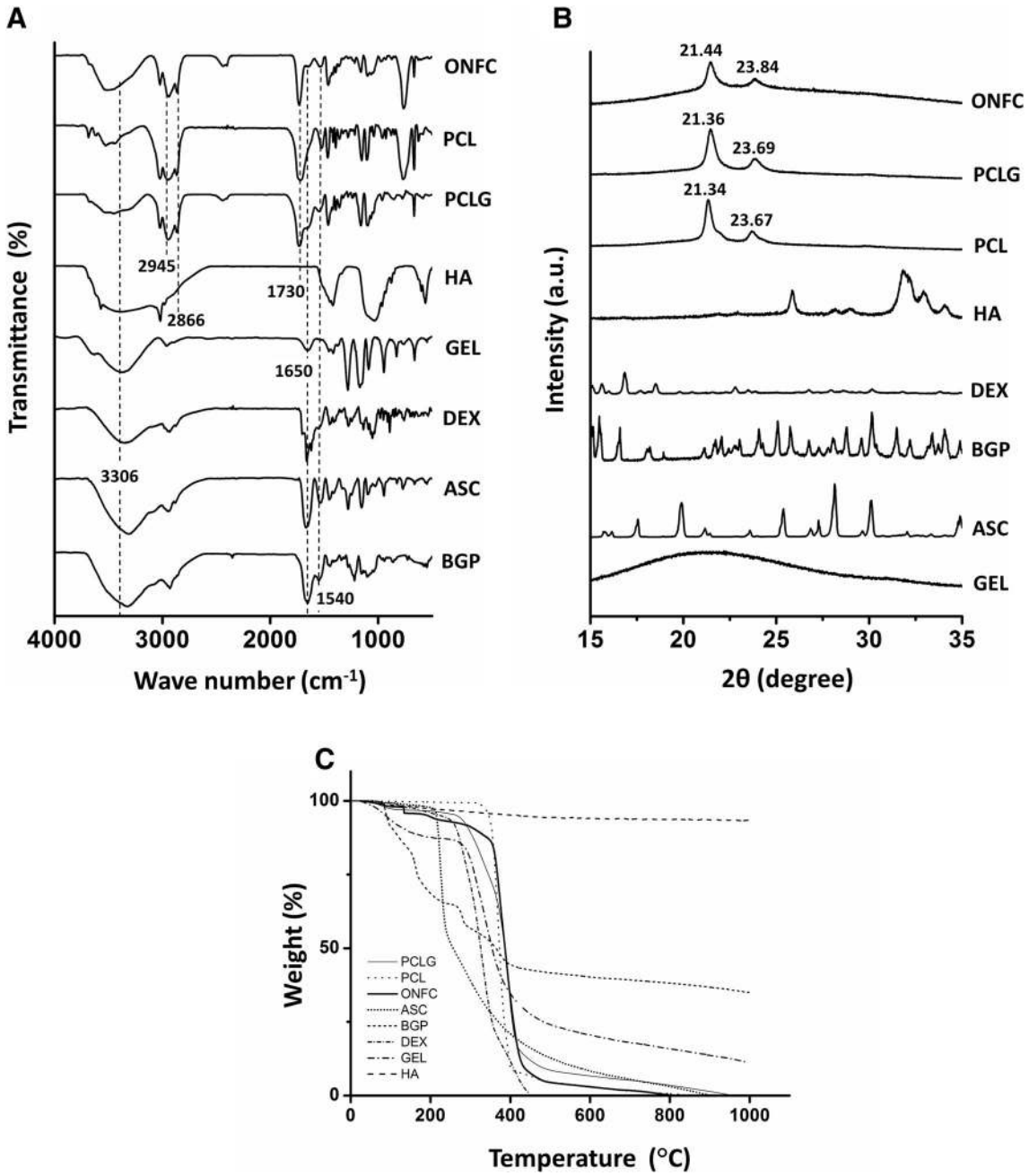

Fig. 3 Characterization of ONFC and its individual components with **A** FTIR, **B** XRD, and **C** TGA. **A** Shows the appearance of the amide groups i.e. 1650 and 1540 cm^{-1} in the FTIR spectra of the ONFC indicating that the PCL chains were chemically bonded to gelatin leading to introduction of functional group such as NH_2, COOH in the nanofibres. The other components doesnot provides significant IR peaks in the ONFC spectra probably due to its limited incorporation in the composite coating. **B** Shows X-ray diffractogram of osteogenic nanofibrous coating (ONFC) and its additives. Shifting of diffraction peaks to higher angles for ONFC is seen suggesting the formation of different crystalline structure. **C** Shows the TGA curves of osteogenic nanofibrous coating (ONFC) and its additives. The thermogram of ONFC shows a distinct two-stage degradation profile confirming the grafting of all components and formation of sterocomplex fibres

gelatin. The band of gelatin appeared at 1650 cm^{-1} (amide I) and 1540 cm^{-1} (amide II). Amide I, the most intense absorption band in proteins is determined by backbone conformation and hydrogen bonding pattern [54].The band of gelatin appeared at 1650 cm^{-1} (amide I) probably be due to the random coil/α-helix structure of gelatin. The characteristics absorption band at 3306 cm^{-1} in association with the NH stretching vibration in gelatin incorporated in the ONFC could be seen in the spectra. The peak at 1730 cm^{-1} which is related to the stretching vibration of

the carbonyl groups associated with the ester bond in PCL is seen in the IR spectra of ONFC.

The XRD of ONFC shows low intensity, semi crystalline diffraction peaks at Bragg's angles $2\theta = 21.44$ and 23.84 which is due to (110) and (200) reflections of PCL present in the ONFC (Fig. 3B) [55]. The pure PCL has a polyethylene-like crystal structure with orthorhombic unit cell parameters where the two prominent peaks are $2\theta = 21.34$ and 23.67 [56]. With the addition of chemicals like gelatin, hydroxyapatite (HA reference peaks, JCPDS card No. 24–33), beta-glycerophosphate, dexamethasone and ascorbic acid the intensity of 2θ decreased with right shift and become amorphous broad peaks for ONFC suggesting the formation of different crystal form and a less ordered structure or a lesser degree of crystallinity in the blend fibres. These data demonstrate that crystal forms and the orientation in the blended polymer fibres are different from those found in pure PCL or PCLG nanofibrous membranes. Further, no prominent diffraction peaks due to presence of hydroxyapatite, dexamethasone, beta-glycerophosphate, ascorbic acid and gelatin could be observed or correlated in ONFC, suggesting that they were all dispersed uniformly and no crystalline clusters of these were present within the polymer blend.

Figure 3C shows the thermogram of ONFC and its components. The TGA curve of ONFC shows two-stage thermal degradation profile with the initial decomposition temperature at 130.47 °C mostly due to breakage of the intermolecular hydrogen bonds and ester pyrolysis induced disruption of polyester chains liberating carboxylic acid group, CO_2 and water along with low molecular mass compounds losing around 2.11% of its total mass [57–59].

The second stage decomposition starts at 350.89 °C mostly due to cleavage of the backbone of the polymer that occurs above 300 °C with protein chain breakage and peptide bond rupture present in the ONFC composites [60]. The thermogram of ONFC shows increase in degradation temperature and a significant shift of weight loss occurs towards higher temperature, approximately 40 °C higher when compared to pure PCL nanofibres suggesting that ONFC have increased thermal stability. This further supports the formation of stereocomplex ONFC [59].

The tensile stress of ONFC was found to be 5.3 ± 0.9 MPa, however for pure PCL nanofibres the tensile stress was 1.6 ± 0.10 MPa (Fig. 4B). The higher tensile strength of ONFC compared to PCL nanofibres may primarily attributed to increase in crosslinking of gelatin and incorporation of osteogenic chemicals. It was reported earlier that increase in gelatin ratio in the PCL nanofibres results in improved mechanical properties and our studies shows complimentary findings [61]. The Young's modulus and percentage elongation for ONFC was found to be 13.96 ± 3.91 MPa and 57.34 ± 6.8 (%) when compared to pure PCL nanofibres with Young's modulus of 4.38 ± 0.60 MPa and percentage elongation of 45.15 ± 2.91 (%) respectively. The combine effect of gelatin and osteogenic chemicals in the nanofibres results in improved values of ONFC when compared with pure PCL nanofibres and is in accordance with other studies [62]. Further, literature suggests that the tensile strength of ONFC could not only support chondrocytes [63] and bone (3.5 MPa for cancellous bone) [64] but also provides adequate stiffness by mimicking ECM in the alveolar bone to regenerate periodontal tissues [65]. Additionally, the nano-architecture of the electrospun fibres of ONFC and PCL nanofibres were analysed by Brunauer–Emmett and Teller (BET) measurements. As shown in the Fig. 5A the N_2 adsorption desorption isotherm for the ONFC shows a type IV isotherm with a type H2 hysteresis according to the IUPAC classification which suggests that ONFC have mostly mesopores. The hysteresis loop may be associated with the capillary condensation in the ONFC. Pore size distribution of ONFC (Fig. 5C) shows that mesopores are in overwhelming majority while macropores are less frequent and are in accordance with our ESEM results. Further, as seen in Fig. 5B, PCL has type III isotherm pattern according to the IUPAC classification and displays a hysteresis loop of H3 in the range of 0.01–0.98. Additionally, the pore size distribution curve of PCL shows cluster of pores ranging around 1.2 and 3.0 nm (Fig. 5D). These results proves that the nanofibrous mat of PCL have mostly mesopores. Hence, we can conclude that although ESEM confirms the presence of macropores, the porous coating of ONFC is mainly dominated by mesopores. Notably, compared with PCL nanofibrous coating (surface area = 12.55 $m^2\ g^{-1}$), ONFC nanofibrous coating (surface area = 12.94 $m^2\ g^{-1}$) demonstrate considerably higher BET specific surface area. Hence, we presume that our ONFC nanofibrous coating with interconnected pores resembling ECM will result in better infiltration of cells and subsequently regeneration of intended tissues [66].

Upon AFM analysis, the ONFC nanofibrous coating exhibited an isotropic terrain of microscaled valleys and ridges corresponding to the texture of non-aligned osteogenic nanofibrous coating having an average roughness of 392 ± 23 nm (Fig. 6A). However, the uncoated pure titanium surface exhibited a smooth surface morphology with roughness of 1.5 ± 0.43 nm which corresponds to previous reported values in the literatures (Fig. 6B) [6]. The topographic profile curves further confirms that ONFC nanofibrous coating have more crests and toughs compared to smooth surface of pure titanium implant which shows a straight line profile in accordance with our ESEM results (Fig. 6C, D). Upon closer inspection of uncoated titanium surface (nano-scale range) the profile curve shows irregular valleys and ridges (1–5 nm) suggesting that titanium

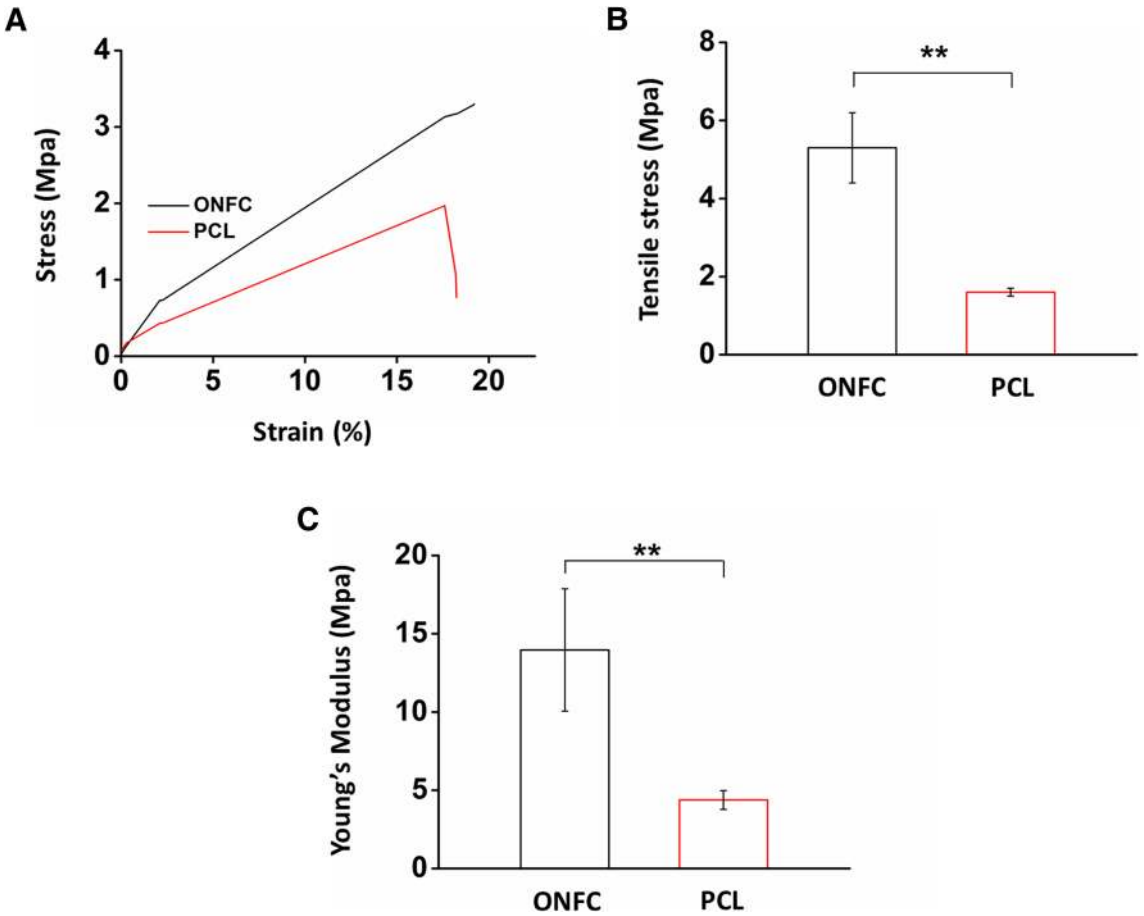

Fig. 4 Mechanical properties of ONFC and PCL nanofibres. **A** Stress versus strain curve of ONFC and PCL nanofibres, **B** Tensile stress of ONFC and PCL nanofibres and **C** Young's modulus of ONFC and PCL nanofibres. ONFC exhibits improved mechanical properties when compared to PCL nanofibres

implant have nano groves and ridges on its surface (data not shown). There are conflicting reports in the literature which suggests an increase in cell adhesion and proliferation with increase roughness [67] while other indicates an existence of optimum range of roughness to evoke a favourable biological response [68]. However, modification of surface topography of titanium implants with roughness comparable to ours i.e. in order of 0.2–0.6 μm showed enhanced adhesion and proliferation of cells [69]. Evaluation of wettability properties (Fig. 6E) reveals that pure PCL nanofibrous coating shows increase magnitude of contact angle i.e. 116° ± 1.9°, displaying hydrophobic surface features which is in good agreement with the previous studies [70, 71]. However, the contact angle of ONFC showed significant lower contact angle i.e. 30.4 ± 2.27 °C due to incorporation of hydrophilic additives like gelatin, hydroxyapatite and ascorbic acid. This result further implies that the additives used in ONFC are successfully grafted to form a homogeneous nanofibres coating. The contact angle of pure titanium implant is 64 ± 2° according to various published reports [46–48]. Literature suggests that moderately hydrophilic surfaces (20–40 degrees water contact angle) like the surface of our ONFC implant promotes the highest levels of cell attachment [72]. In continuance with the above discussion, the cytotoxic and biocompatibility evaluation of ONFC was compared to PCL nanofibres which is a well-established biocompatible material. We found no significant difference in the amount of fluorescence due to reduced resorufin as depicted in the Fig. 6F. The standard curve obtained shows a time related increase in resorufin indicating that the culturing cells in the ONFC are not detrimental to cell viability.

For examining the biomineralization activity, the images of ONFC evaluated after 7th day showed sporadic bioactivity in forming crystals (Fig. 7A). The ESEM image of the ONFC sample of the 14th day showed random mineralized cluster areas along the surfaces of fibre network (Fig. 7C). However, on examining the ESEM images on 21st day, ONFC was found to be completely covered with packed petal-like grains (Fig. 7E). The densely packed polygonal nanocrystals were similar to the clusters of

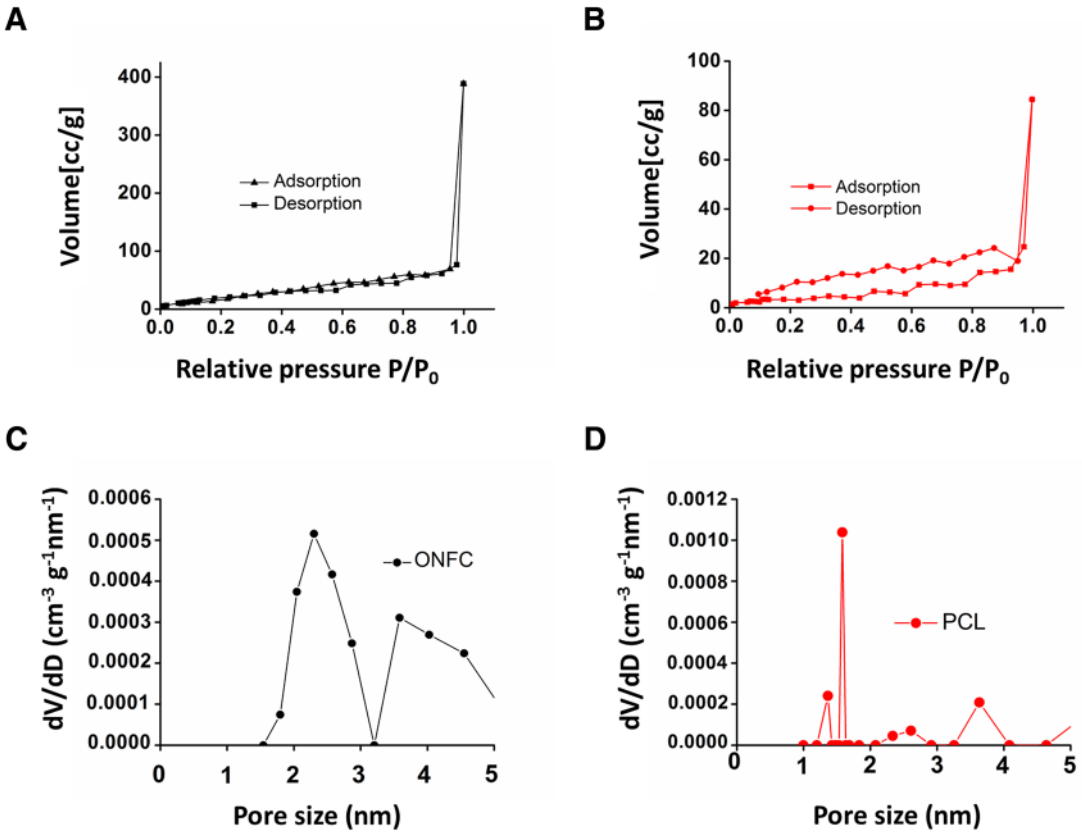

Fig. 5 Surface area and pore analysis. **A** Nitrogen adsorption–desorption isotherm for ONFC, **B** PCL nanofibres. **C** Pore diameter analysis by BJH theory for ONFC and **D** PCL nanofibres. ONFC exhibits mostly mesopores and have comparable pore size and pore volume to that of PCL nanofibres

mineral precipitates and resembles the structure of secondary bone ECM. The EDX results of ONFC after immersion in SBF confirmed the presence of calcium and phosphorous on the surface of the deposited layer (Fig. 7B, D, F). The Ca/P molar ratio of all the samples (n = 3) ranged from 1.41 to 1.52 which is close to that of stoichiometric hydroxyapatite (Ca/P = 1.67), proving that the layer formed after soaking in SBF for 7,14 and 21 days are indeed the apatite layer. Hence, it could be inferred that the ONFC was initiating the mineralization process and promoting crystal growth. In contrast, the ESEM and EDX analysis revealed that the plain PCL nanofibrous scaffold does not support heterogeneous calcium phosphate nucleation and growth. The scaffold surface appeared to be smooth after immersion in SBF for 7 days (Fig. 7G). The ESEM images of PCL nanofibres (14th and 21th day) showed few apatite nanoparticles indicating PCL nanofibres does not induce mineralization *in vitro* (Fig. 7I, K). The EDX analysis further affirm the conclusion (Fig. 7H, J, L). Apatite crystal formation on the surface of the coated implant body in the SBF solution, is a clear indication of the potential of ONFC to facilitate bone growth and osseointegration (Table 1).

Table 1 EDX analysis of crystals grown on ONFC implant in SBF after 21 days of incubation

Element	Weight %	Atomic %	K-ratio
Carbon	16.28	29.65	0.0278
Oxygen	24.50	33.51	0.0337
Sodium	1.06	1.01	0.0038
Magnesium	0.89	0.80	0.0046
Phosphorus	22.45	15.86	0.1889
Chlorine	2.13	1.32	0.0169
Potassium	0.48	0.27	0.0043
Calcium	32.21	17.58	0.2937

3.2 *In vivo* study

The micro-CT images as seen in Fig. 8 confirms that the occurrence related to healing of bone followed by osseointegration for both ONFC and control implants occurred uneventfully. Examination of micro-CT images revealed direct contact of newly formed bone with both ONFC and uncoated titanium implants. The cortical diaphysis of tibia displays gradual widening at the contact

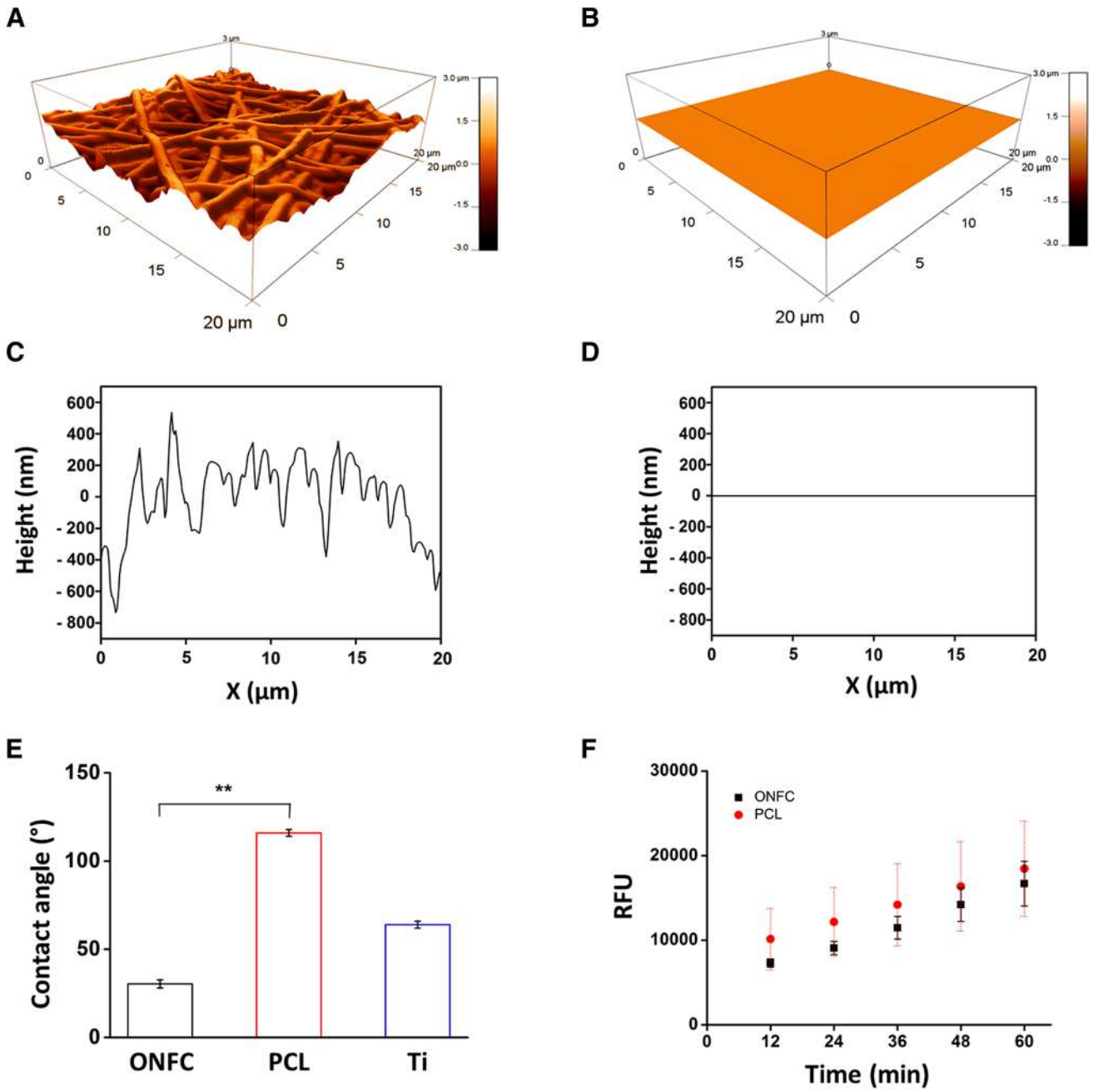

Fig. 6 Surface characterization by AFM (**A–D**), contact angle (**E**) and biocompatibility evaluation (**F**). **A** Topographical feature of osteogenic nanofibrous coated (ONFC) implant, **B** uncoated implant, **C** height profile of ONFC titanium implant and **D** uncoated implant. AFM analysis reveals ONFC implant have more surface area and roughness compared to uncoated titanium implant. **E** Water contact angle of ONFC, PCL nanofibres and (Ti) titanium implant surfaces is shown. ONFC exhibits hydrophilic features. **F** Resazurin assay for measuring cell viability in ONFC and PCL nanofibres. No statistical significant difference was observed between test and control confirming that ONFC is nontoxic and have biocompatible features

area of the implants suggesting successful bone integration of implants. Close inspection of the implants in the sagittal plane reveals radiopaque cortical plates approximating the ONFC and control implant surface. However, unlike the ONFC implant which shows uniform and homogeneous contact, the control implants have a non-uniform approximation of cortical plates displaying some radiolucent voids in the bone-implant interface suggesting an inferior grade of osseointegration compared to ONFC implant.

When compared to interface of control implants, the ONFC implants have higher contact ratio. The BMD and BMC were higher in ONFC implants i.e. 14.39 and 27.62% respectively when compared to control. The BMD

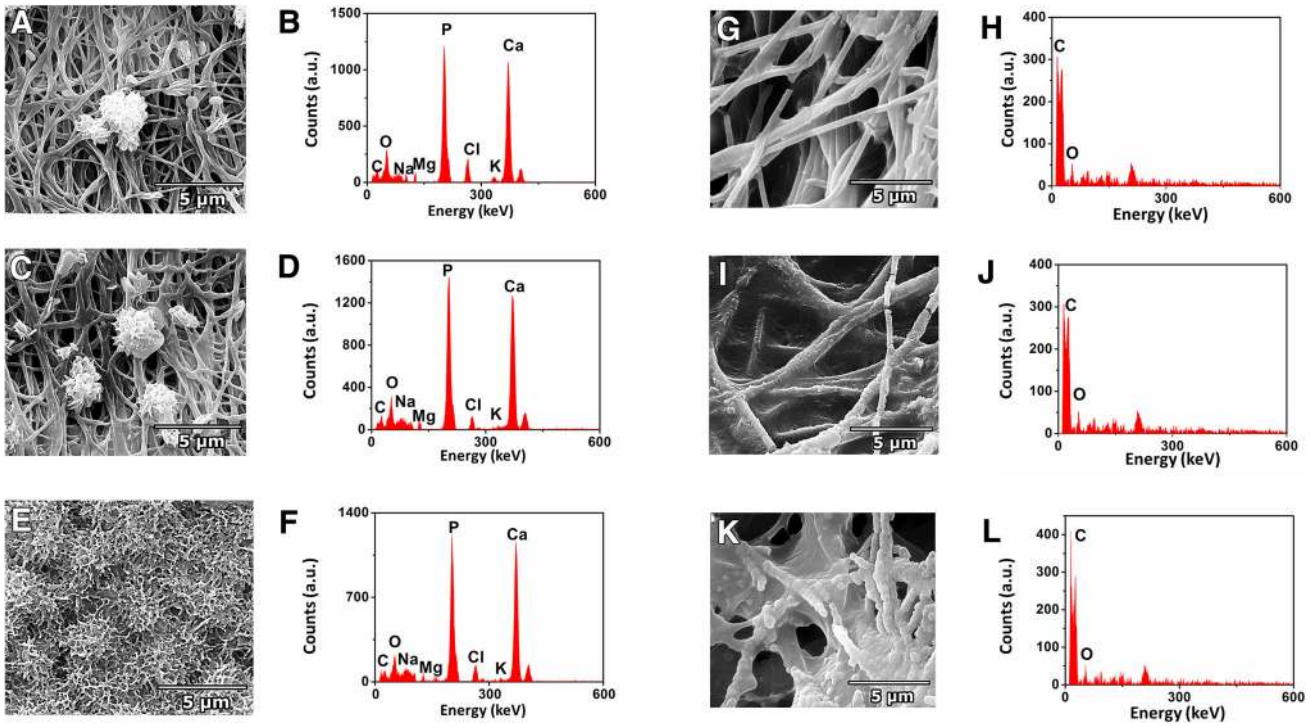

Fig. 7 ESEM images and EDX analysis of SBF treated ONFC and PCL nanofibres on 7th, 14th and 21st day. ESEM and EDX of ONFC after **A**, **B** 7th, **C**, **D** 14th and **E**, **F** 21st day confirms biomineralization activity. However, no apatite formation was noted in SBF treated PCL nanofibres after **G**, **H** 7th, **I**, **J** 14th and **K**, **L** 21st day. Hence, ONFC was initiating the mineralization process and promoting crystal growth

(1070.40 ± 89.28 mg/cc) and BMC (1163.54 ± 290.52 mg) of ONFC implant were almost comparable to BMD and BMC of normal bone i.e. left (1339.26 ± 86.79 mg/cc and 1058.38 ± 68.59 mg) and right tibia (1279.52 ± 44.78 mg/cc and 841.26 ± 128.085 mg) (non-implanted site) respectively suggesting an enhanced osteogenesis induced by ONFC implants (Fig. 9).

To quantify the growth of osseous tissue on the ONFC and control implant following approaches were explored.

1. The cortical thickness of bone at various sites were measured to quantify the regenerated osseous tissue. Briefly, in axial and sagittal planes, the length of cortical bones were measured proximally i.e. on either side of the control and ONFC implant–bone interface respectively. The mid-level of implant was also taken into consideration. (Table 2).
2. The regenerated bone was also assessed by calculating implant bone integrated volume (IBIV). It is defined as 3D volume of implant with circumscribed regenerated osseous tissue approximately 1.5 mm from centre of the long axis of the implant (Table 3a, b).

The analysis of BMD and BMC values, IBIV and length of cortical bones used for characterization of osseous state in response to ONFC and control implant disclose an increase in their respective values over the control level, 6 weeks post-implantation. The observation may be explained by the fact that osteogenic chemicals incorporated in the ONFC mimicking bone ECM may stimulate interaction of osteoblast and mesenchymal stem cells present in the immediate peri-implant tissue with those present in distal tissues resulting in initiation of cascading events like cell attachment, migration and proliferation, differentiation of stem cells, synthesis of extracellular matrix and local factor production ultimately resulting in incorporation of the implant is the osseous tissue. The osteogenic environment is probably initiated by autocrine/paracrine effects of these local factors. Similarly, the cells located away from the implant surface are also capable of exerting an influence via autocrine/paracrine pathway [73]. Therefore, we believe that enhanced regeneration of osseous tissue could be the result of the induced differentiation of the mesenchymal stem cells by virtue of our ONFC implant.

Histological examination reveals neo-osseous tissue with well-defined architecture in mesial and distal surfaces for both ONFC and control implants. The histological images doesnot indicate the incidence of inflammation, immune response, tissue necrosis or osteolysis 6 weeks post-implantation for both type of implants. Mainly, cortical bone was observed surrounding the implants. Occasionally, sporadic islands of fibrous tissue persists at the interfaces for both type of implants which are in the

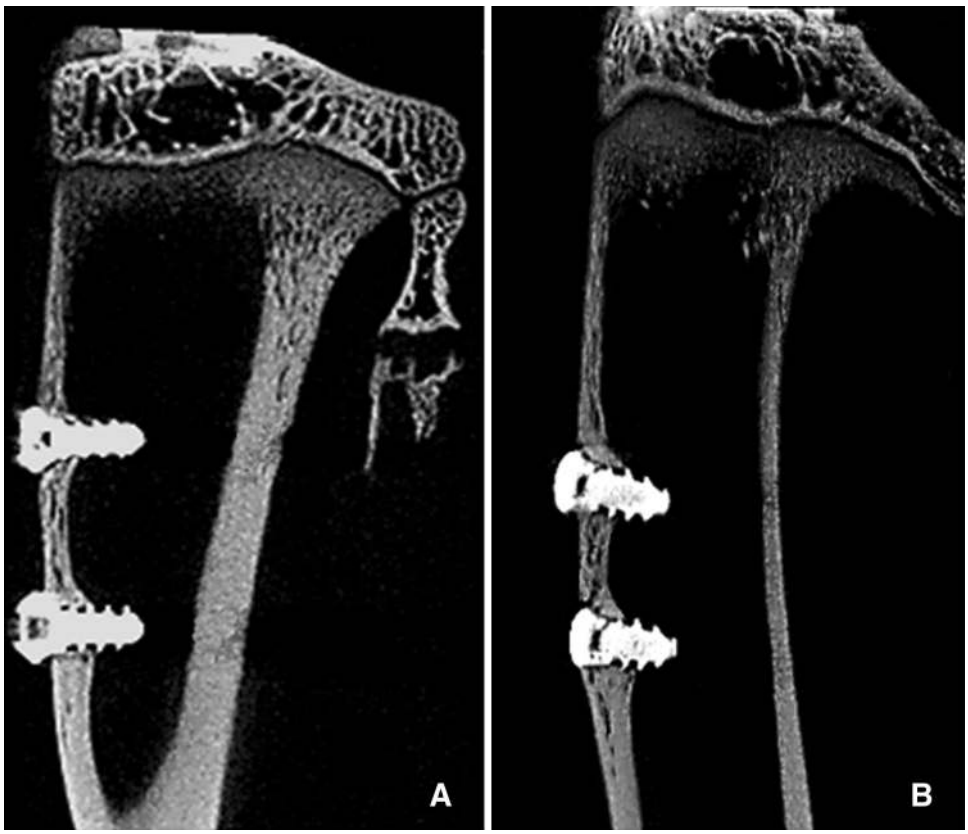

Fig. 8 Micro-computed tomography (micro-CT) images of **A** ONFC implants and **B** control implants in tibial diaphysis of a rabbit model. The bone-implant interface of ONFC implant shows higher degree of homogenous approximation of cortical bone when compared to control implant

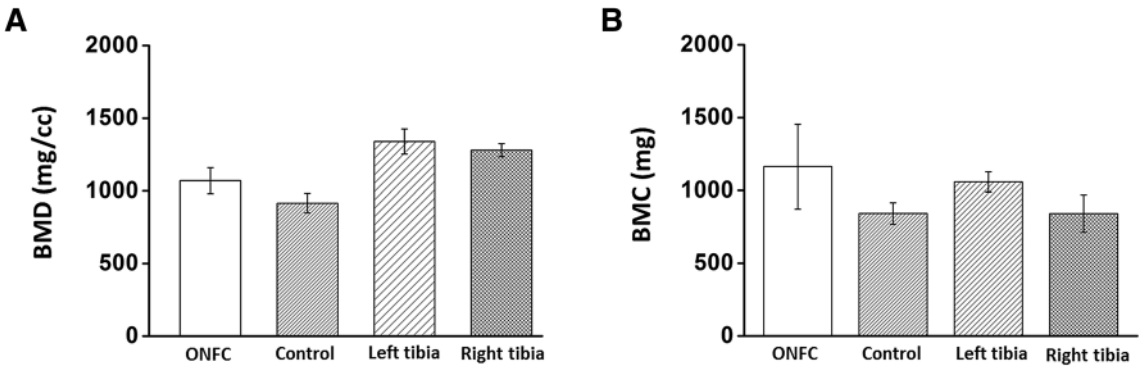

Fig. 9 **A** Bone mineral density (BMD) and **B** bone mineral content (BMC) of ONFC and control implant. The regenerated osseous tissue circumscribing the ONFC implant have higher bone mineral density and bone mineral content when compared to control implant

process of being gradually replaced by woven bone. New woven bone and lamellar bone are extensively seen. The ONFC has been degraded during the metabolic process. On close inspection, mature bone deposition is seen on the surface of the ONFC implant. The spreading of osseous tissue into the flank and root space of the ONFC implant is noticeably higher when compared to control implant at the end of 6 weeks post implantation (Fig. 10).

In general, it can be stated that in ONFC implants, pore size distribution coupled with surface properties resulted in fabrication of favourable topographical substratum yielding accentuated bio-response of mesenchymal stem cells and osteoblasts in the peri-implant zone. The moderately hydrophilic surface feature along with mechanical properties of the biodegradable coating contributed equally for enhanced osseointegration of implant. The intrinsic bioactivity and viability assay of ONFC implant further corroborated the *in vivo* results.

Our preliminary study showed that micro-CT findings had significant correlation with histological study on undecalcified bone specimen for *in vivo* quantification of peri-implant osseous microstructure. For comparative study, we choose ROI $\sim$ 0.5–1 mm from the surface of the implant. The comparisons between ONFC and control

Table 2 Length of cortical bone in axial plane, sagittal plane and on mid-level of implant along with mesial and distal side of bone-implant interface

Axial plane		Sagittal plane	
Length of ONFC bone-implant interface on mesial side (Implant no. 1)	1.99 ± 0.05 mm	Length of ONFC bone-implant interface on mesial side (Implant no. 1)	1.93 ± 0.03 mm
Length of ONFC bone implant interface on distal side (Implant no. 1)	1.83 ± 0.03 mm	Length of ONFC bone-implant interface on distal side (Implant no. 1)	2.01 ± 0.03 mm
Mid level of ONFC implant (Implant no. 1)	2.09 ± 0.02 mm	Mid level of ONFC implant (Implant no. 1)	1.89 ± 0.02 mm
Length of ONFC bone-implant interface on mesial side (Implant no. 2)	2.16 ± 0.04 mm	Length of ONFC bone-implant interface on mesial side (Implant no. 2)	1.6 ± 0.02 mm
Length of ONFC bone-implant interface on distal side (Implant no. 2)	2.0 ± 0.02 mm	Length of ONFC bone-implant interface on distal side (Implant no. 2)	1.72 ± 0.04 mm
Mid level of ONFC implant (Implant no. 2)	2.12 ± 0.05 mm	Mid level of ONFC implant (Implant no. 2)	1.71 ± 0.06 mm
Length of control bone-implant interface on mesial side (Implant no. 1)	1.06 ± 0.04 mm	Length of control bone-implant interface on mesial side (Implant no. 1)	2.05 ± 0.06 mm
Length of control bone-implant interface on distal side (Implant no. 1)	1.11 ± 0.03 mm	Length of control bone-implant interface on distal side (Implant no. 1)	1.6 ± 0.05 mm
Mid level of control implant (Implant no. 1)	1.2 ± 0.08 mm	Mid level of control implant (Implant no. 1)	2.1 ± 0.09 mm
Length of control bone-implant interface on mesial side (Implant no. 2)	1.17 ± 0.05 mm	Length of control bone-implant interface on mesial side (Implant no. 2)	1.35 ± 0.02 mm
Length of control bone-implant interface on distal side (Implant no. 2)	1.44 ± 0.08 mm	Length of control bone-implant interface on distal side (Implant no. 2)	1.14 ± 0.03 mm
Mid level of control implant (Implant no. 2)	1.5 ± 0.04 mm	Mid level of control implant (Implant no. 2)	1.5 ± 0.13 mm

Table 3 (a) Implant bone integrated volume (IBIV) in axial plane, (b) Implant bone integrated volume (IBIV) in sagittal plane

	ONFC		Control	
	Mesial	Distal	Mesial	Distal
(a) *Evaluation of implant bone integrated volume (IBIV) in axial plane* (mm^3)				
Implant 1	8.02 ± 0.50	6.97 ± 0.49	4.31 ± 0.03	4.45 ± 0.02
Implant 2	0.06 ± 0.01	0.074 ± 0.002	4.46 ± 0.03	4.37 ± 0.01
(b) *Evaluation of implant bone integrated volume (IBIV) in sagittal plane* (mm^3)				
Implant 1	0.25 ± 0.01	0.26 ± 0.005	0.06 ± 0.004	0.08 ± 0.002
Implant 2	0.33 ± 0.07	0.33 ± 0.01	0.04 ± 0.003	0.06 ± 0.01

analyses showed highly significant correlation and good agreement between micro-CT, histological photomicrograph and our *in vitro* results. Interestingly, the IBIV of one of the ONFC implant (implant no. 2) was significantly low (Table 3a, b). We ascribe this to the fact that ONFC coating was detached and separated from this implant surface during surgical placement due to sudden pedal reflex of rabbit. The remnants of crumpled and creased nanofibrous coating probably interfered with osteogenesis and might have some inhibitory effect in bone formation. It have been, reported earlier in the literature that physical structure of the biomaterial plays a crucial role in extracellular matrix production and have significant effect in osteoblastic differentiation of mesenchymal stem cells [74, 75]. Hence, caution should be taken during placement of such coated implants. A major limitation in the present study exists due to the use of only four implants in each condition being investigated. Hence, we cannot establish with absolute certainty about the osteogenic potentials of ONFC implant. However, the micro-CT and histological results clearly demonstrate that the ONFC implant results in enhanced bone integration. Therefore, there is a higher possibility of clinical use of our ONFC implants after a more detailed and elaborate study, which is underway.

In conclusion, bioactive ONFC implants were found to surpass the uncoated titanium implant in conventional micro-CT and histological evaluation. The overall findings of this study infers that titanium implants with ONFC to be

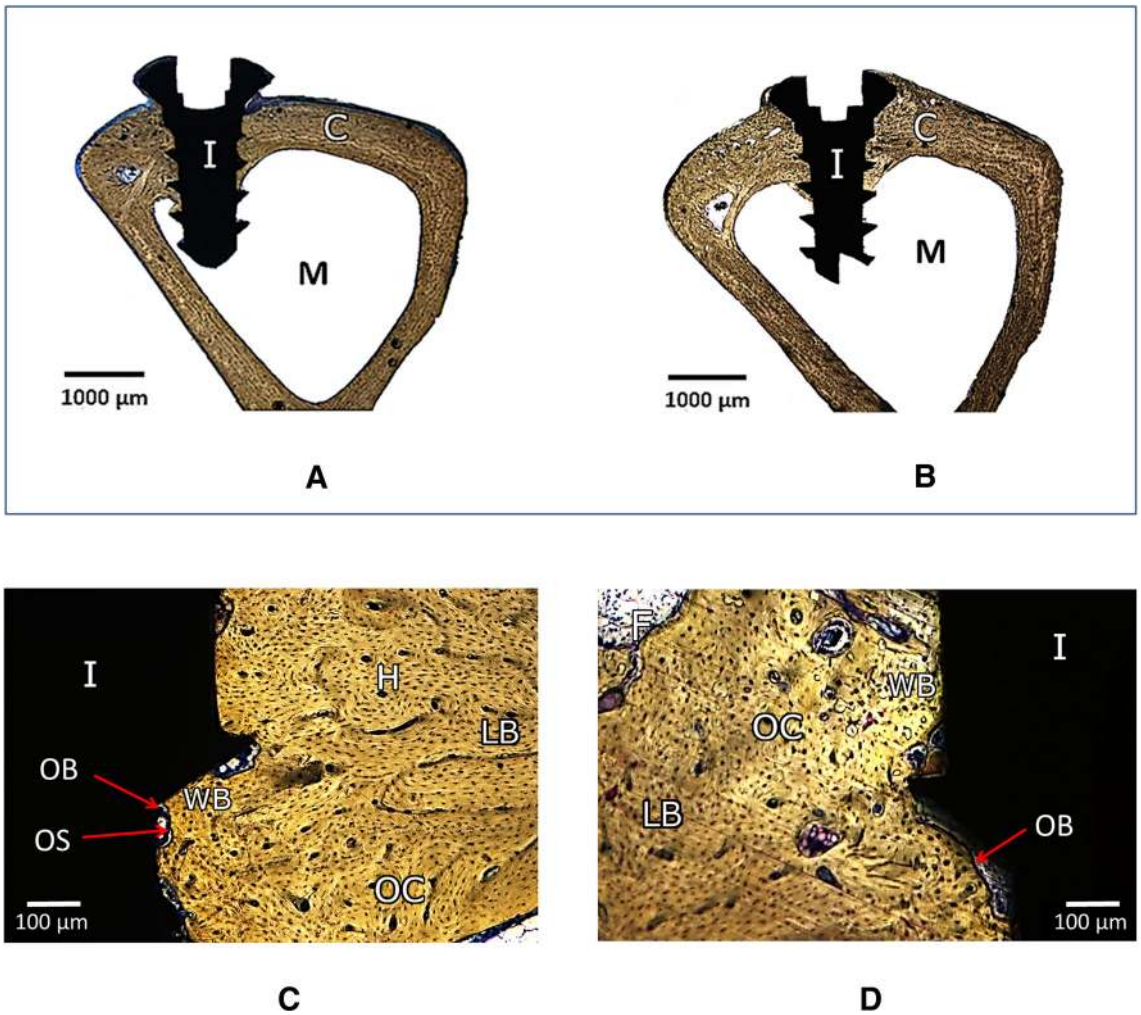

Fig. 10 Histological evaluation: Low magnification of resin section of **A** ONFC and **B** control implant in bone is seen. In both types, cortical bone (C) is seen all around the implant (I) in the implant site and marrow cavity (M) at the center. **C** and **D** shows tissue response to ONFC and control implant in bone at higher magnification respectively. In ONFC implant, good and early mature bone deposition is seen at the interface. Fibrous tissue (F) being replaced by new woven bone (WB) at the interface. Mature lamellar host bone (LB) is well demarcated from new woven bone (WB) adjacent to the implant (I) surface. Osteoblasts (OB) lines the osteoid layer (OS) adjacent to the new bone. Osteoblast embedded in the new bone matrix known as osteocytes (OC) are noted far from the interface. Numerous small Haversian canals (H) are observed. In control implant, mature lamellar host bone (LB) is well demarcated from new woven bone (WB) adjacent to the implant surface (I). Arrows point to osteoblasts (OB), osteocytes (OC) and fibrous tissue (F) seen in new bone. However, the inherent limitation of using single dye restricts the apparent visualization of other biological structures

an efficient alternative to commercially available metallic implants.

Acknowledgements Authors would like to acknowledge IRCC, IIT Bombay for providing SEM, XRD and AFM facilities.

Compliance with ethical standards

Conflict of interest Authors declare that they have no conflict of interests.

Ethical statement The research protocol was reviewed and approved by the panel of ethics committee for laboratory animal research of ACTREC, Navi Mumbai WIHC/3596—TMH-IITB-ACTREC (Animal study proposal no. 03/2016) and was performed as per the guidelines of the Committee for the Purpose of Control and Supervision of Experiments on Animals (CPCSEA), Ministry of Social Justice and Empowerment, Government of India.

Abbreviations

ONFC	Osteogenic nanofibrous coating
PCL	Polycaprolactone
PCLG	Polycaprolactone-gelatin
HA	Hydroxyapatite
GEL	Gelatin
DEX	Dexamethasone
ASC	Ascorbic acid
BGP	Beta-glycerophosphate
SBF	Simulated body fluid

ECM	Extracellular matrix
MSCs	Mesenchymal stem cells
BMD	Bone mineral density
BMC	Bone mineral content
IBIV	Implant bone integrated volume

References

1. Misch CE. Dental implant prosthetics, 2nd ed. Amsterdam: Elsevier Health Sciences; 2014.
2. Brånemark PI, Hansson BO, Adell R, Breine U, Lindström J, Hallén O, et al. Osseointegrated implants in the treatment of the edentulous jaw. Experience from a 10-year period. Scand J Plast Reconstr Surg Suppl. 1977;16:1–132.
3. Kasemo B. Biological surface science. Surf Sci. 2002;500: 656–77.
4. Brunski JB. In vivo bone response to biomechanical loading at the bone/dental–implant interface. Adv Dent Res. 1999;13:99–119.
5. Rosengren A, Danielsen N, Bjursten LM. Inflammatory reaction dependence on implant localization in rat soft tissue models. Biomaterials. 1997;18:979–87.
6. Black J, Hastings G. Handbook of biomaterial properties. Berlin: Springer Science & Business Media; 2013.
7. Lindquist LW, Carlsson GE, Jemt T. A prospective 15-year follow-up study of mandibular fixed prostheses supported by osseointegrated implants. Clinical results and marginal bone loss. Clin Oral Implant Res. 1996;7:329–36.
8. Brunski JB. Biomechanical factors affecting the bone-dental implant interface. Clin Mater. 1992;10:153–201.
9. Martin JY, Schwartz Z, Hummert TW, Schraub DM, Simpson J, Lankford J Jr, et al. Effect of titanium surface roughness on proliferation, differentiation, and protein synthesis of human osteoblast-like cells (MG63). J Biomed Mater Res A. 1995;29: 389–401.
10. Rupp F, Gittens RA, Scheideler L, Marmur A, Boyan BD, Schwartz Z, et al. A review on the wettability of dental implant surfaces I: theoretical and experimental aspects. Acta Biomater. 2014;10:2894–906.
11. Gittens RA, Scheideler L, Rupp F, Hyzy SL, Geis-Gerstorfer J, Schwartz Z, et al. A review on the wettability of dental implant surfaces II: biological and clinical aspects. Acta Biomater. 2014;10:2907–18.
12. Elias CN, Oshida Y, Lima JH, Muller CA. Relationship between surface properties (roughness, wettability and morphology) of titanium and dental implant removal torque. J Mech Behav Biomed Mater. 2008;1:234–42.
13. Massaro C, Rotolo P, De Riccardis F, Milella E, Napoli A, Wieland M, et al. Comparative investigation of the surface properties of commercial titanium dental implants. Part I: chemical composition. J Mater Sci Mater Med. 2002;13:535–48.
14. Kasemo B, Lausmaa J. Surface science aspects on inorganic biomaterials. CRC Crit Rev Clin Neurobiol. 1986;4:335–380.
15. Ito Y, Kajihara M, Imanishi Y. Materials for enhancing cell adhesion by immobilization of cell-adhesive peptide. J Biomed Mater Res. 1991;25:1325–37.
16. Krukowski M, Shively RA, Osdoby P, Eppley BL. Stimulation of craniofacial and intramedullary bone formation by negatively charged beads. J Oral Maxillofac Surg. 1990;48:468–75.
17. Baier RE, Meyer AE. Implant surface preparation. Int J Oral Maxillofac Implants 1988;3:9–20.
18. Bidan CM, Kommareddy KP, Rumpler M, Kollmannsberger P, Bréchet YJ, Fratzl P, et al. How linear tension converts to curvature: geometric control of bone tissue growth. PLoS One. 2012;7:e36336.
19. Bidan CM, Kommareddy KP, Rumpler M, Kollmannsberger P, Fratzl P, Dunlop JW. Geometry as a factor for tissue growth: towards shape optimization of tissue engineering scaffolds. Adv Healthc Mater. 2013;2:186–94.
20. Zadpoor AA. Bone tissue regeneration: the role of scaffold geometry. Biomater Sci. 2015;3:231–45.
21. Wennerberg A, Albrektsson T. Effects of titanium surface topography on bone integration: a systematic review. Clin Oral Implant Res. 2009;20:172–84.
22. Abrahamsson I, Berglundh T, Linder E, Lang NP, Lindhe J. Early bone formation adjacent to rough and turned endosseous implant surfaces. Clin Oral Implant Res. 2004;15:381–92.
23. Kim H, Choi SH, Ryu JJ, Koh SY, Park JH, Lee IS. The biocompatibility of SLA-treated titanium implants. Biomed Mater. 2008;3:025011.
24. Jemat A, Ghazali MJ, Razali M, Otsuka Y. Surface modifications and their effects on titanium dental implants. BioMed Res Int. 2015;2015:791725.
25. Yang GL, He FM, Yang XF, Wang XX, Zhao SF. Bone responses to titanium implants surface-roughened by sandblasted and double etched treatments in a rabbit model. Oral Surg Oral Med Oral Pathol Oral Radiol Endod. 2008;106:516–24.
26. Cho SA, Park KT. The removal torque of titanium screw inserted in rabbit tibia treated by dual acid etching. Biomaterials. 2003;24:3611–7.
27. Kwak HB, Kim JY, Kim KJ, Choi M-K, Kim JJ, Kim KM, et al. Risedronate directly inhibits osteoclast differentiation and inflammatory bone loss. Biol Pharm Bull. 2009;32:1193–8.
28. Elliott SN, McKnight W, Davies NM, MacNaughton WK, Wallace JL. Alendronate induces gastric injury and delays ulcer healing in rodents. Life Sci. 1998;62:77–91.
29. Frantz C, Stewart KM, Weaver VM. The extracellular matrix at a glance. J Cell Sci. 2010;123:4195–200.
30. Badylak SF, Freytes DO, Gilbert TW. Extracellular matrix as a biological scaffold material: structure and function. Acta Biomater. 2009;5:1–13.
31. Moore KA, Lemischka IR. Stem cells and their niches. Science. 2006;311:1880–5.
32. Wang X, Ding B, Li B. Biomimetic electrospun nanofibrous structures for tissue engineering. Mater Today (Kidlington). 2013;16:229–41.
33. Greiner A, Wendorff JH. Electrospinning: a fascinating method for the preparation of ultrathin fibers. Angew Chem Int Ed Engl. 2007;46:5670–703.
34. Li WJ, Laurencin CT, Caterson EJ, Tuan RS, Ko FK. Electrospun nanofibrous structure: a novel scaffold for tissue engineering. J Biomed Mater Res. 2002;60:613–21.
35. Hwang PT, Murdock K, Alexander GC, Salaam AD, Ng JI, Lim DJ, et al. Poly(ε-caprolactone)/gelatin composite electrospun scaffolds with porous crater-like structures for tissue engineering. J Biomed Mater Res A. 2016;104:1017–29.
36. Langenbach F, Handschel J. Effects of dexamethasone, ascorbic acid and β-glycerophosphate on the osteogenic differentiation of stem cells in vitro. Stem Cell Res Ther. 2013;4:117.
37. Hamidouche Z, Haÿ E, Vaudin P, Charbord P, Schüle R, Marie PJ, et al. FHL2 mediates dexamethasone-induced mesenchymal cell differentiation into osteoblasts by activating Wnt/β-catenin signaling-dependent Runx2 expression. FASEB J. 2008;22:3813–22.
38. Phillips JE, Gersbach CA, Wojtowicz AM, García AJ. Glucocorticoid-induced osteogenesis is negatively regulated by Runx2/Cbfa1 serine phosphorylation. J Cell Sci. 2006;119:581–91.

39. Jaiswal N, Haynesworth SE, Caplan AI, Bruder SP. Osteogenic differentiation of purified, culture-expanded human mesenchymal stem cells in vitro. J Cell Biochem. 1997;64:295–312.
40. Woodard JR, Hilldore AJ, Lan SK, Park CJ, Morgan AW, Eurell JA, et al. The mechanical properties and osteoconductivity of hydroxyapatite bone scaffolds with multi-scale porosity. Biomaterials. 2007;28:45–54.
41. Imaizumi H, Sakurai M, Kashimoto O, Kikawa T, Suzuki O. Comparative study on osteoconductivity by synthetic octacalcium phosphate and sintered hydroxyapatite in rabbit bone marrow. Calcif Tissue Int. 2006;78:45–54.
42. Pepla E, Besharat LK, Palaia G, Tenore G, Migliau G. Nano-hydroxyapatite and its applications in preventive, restorative and regenerative dentistry: a review of literature. Ann Stomatol (Roma). 2014;5:108–14.
43. Wang B, Chang E, Yang C, Tu D. A histomorphometric study on osteoconduction and osseointegration of titanium alloy with and without plasma-sprayed hydroxyapatite coating using back-scattered electron images. J Mater Sci Mater Med. 1993;4: 394–403.
44. Wise DL, Trantolo DJ, Altobelli DE, Yaszemski MJ, Gresser JD. Human biomaterials applications. Berlin: Springer Science & Business Media; 2013.
45. Jarcho M. Calcium phosphate ceramics as hard tissue prosthetics. Clin Orthop Relat Res. 1981;157:259–78.
46. Fischer K, Kühnert M, Gläser R, Schulze A. Photocatalytic degradation and toxicity evaluation of diclofenac by nanotubular titanium dioxide–PES membrane in a static and continuous setup. RSC Adv. 2015;5:16340–8.
47. He S, Zhou P, Wang L, Xiong X, Zhang Y, Deng Y, et al. Antibiotic-decorated titanium with enhanced antibacterial activity through adhesive polydopamine for dental/bone implant. J R Soc Interface. 2014;11:20140169.
48. Strnad G, Chirila N, Petrovan C, Russu O. Contact angle measurement on medical implant titanium based biomaterials. Procedia Technol. 2016;22:946–53.
49. Kokubo T, Kushitani H, Sakka S, Kitsugi T, Yamamuro T. Solutions able to reproduce in vivo surface-structure changes in bioactive glass-ceramic A-W. J Biomed Mater Res. 1990;24:721–34.
50. Baji A, Mai YW, Wong SC, Abtahi M, Chen P. Electrospinning of polymer nanofibers: effects on oriented morphology, structures and tensile properties. Compos Sci Technol. 2010;70:703–18.
51. Ratanavaraporn J, Rangkupan R, Jeeratawatchai H, Kanokpanont S, Damrongsakkul S. Influences of physical and chemical crosslinking techniques on electrospun type A and B gelatin fiber mats. Int J Biol Macromol. 2010;47:431–8.
52. McMurry J, Castellion M, Ballantine DS, Hoeger CA, Peterson VE. Fundamentals of general, organic, and biological chemistry. London: Pearson Education; 2010.
53. McMurry J, Begley TP. The organic chemistry of biological pathways. Englewood: Roberts and Company Publishers; 2005.
54. Bandekar J, Krimm S. Vibrational analysis of peptides, polypeptides, and proteins: characteristic amide bands of β-turns. Proc Natl Acad Sci U S A. 1979;76:774–7.
55. Yeo MG, Kim GH. Preparation and characterization of 3D composite scaffolds based on rapid-prototyped PCL/β-TCP struts and electrospun PCL coated with collagen and HA for bone regeneration. Chem Mater. 2012;24:903–13.
56. Meng ZX, Zheng W, Li L, Zheng YF. Fabrication and characterization of three-dimensional nanofiber membrance of PCL–MWCNTs by electrospinning. Mater Sci Eng C Mater Biol Appl. 2010;30:1014–21.
57. Fukushima K, Tabuani D, Camino G. Nanocomposites of PLA and PCL based on montmorillonite and sepiolite. Mater Sci Eng C Mater Biol Appl. 2009;29:1433–41.
58. Lebourg M, Martínez-Díaz S, García-Giralt N, Torres-Claramunt R, Gómez-Tejedor JA, Ribelles JL, et al. Cell-free cartilage engineering approach using hyaluronic acid-polycaprolactone scaffolds: a study in vivo. J Biomater Appl. 2014;28:1304–15.
59. Goonoo N, Bhaw-Luximon A, Rodriguez I, Wesner D, Schönherr H, Bowlin GL, et al. Poly(ester–ether)s: III. Assessment of cell behaviour on nanofibrous scaffolds of PCL, PLLA and PDX blended with amorphous PMeDX. J Mater Chem B. 2015;3: 673–87.
60. Bajsić EG, Bulatović VO, Slouf M, Šitum A. Characterization of biodegradable polycaprolactone containing titanium dioxide micro and nanoparticles. Int J Chem Nucl Mater Metall Eng. 2014;8:611–5.
61. Yao R, He J, Meng G, Jiang B, Wu F. Electrospun PCL/gelatin composite fibrous scaffolds: mechanical properties and cellular responses. J Biomater Sci Polym Ed. 2016;27:824–38.
62. Kim MS, Jun I, Shin YM, Jang W, Kim SI, Shin H. The development of genipin-crosslinked poly(caprolactone) (PCL)/gelatin nanofibers for tissue engineering applications. Macromol Biosci. 2010;10:91–100.
63. Skotak M, Noriega S, Larsen G, Subramanian A. Electrospun cross-linked gelatin fibers with controlled diameter: the effect of matrix stiffness on proliferative and biosynthetic activity of chondrocytes cultured in vitro. J Biomed Mater Res A. 2010;95:828–36.
64. Damien CJ, Parsons JR. Bone graft and bone graft substitutes: a review of current technology and applications. J Appl Biomater. 1991;2:187–208.
65. Bottino MC, Thomas V, Janowski GM. A novel spatially designed and functionally graded electrospun membrane for periodontal regeneration. Acta Biomater. 2011;7:216–24.
66. Nam J, Huang Y, Agarwal S, Lannutti J. Improved cellular infiltration in electrospun fiber via engineered porosity. Tissue Eng. 2007;13:2249–57.
67. Loesberg WA, te Riet J, van Delft FC, Schön P, Figdor CG, Speller S, et al. The threshold at which substrate nanogroove dimensions may influence fibroblast alignment and adhesion. Biomaterials. 2007;28:3944–51.
68. Dalby MJ, Riehle MO, Johnstone H, Affrossman S, Curtis AS. In vitro reaction of endothelial cells to polymer demixed nanotopography. Biomaterials. 2002;23:2945–54.
69. Schwartz Z, Raz P, Zhao G, Barak Y, Tauber M, Yao H, et al. Effect of micrometer-scale roughness of the surface of Ti6Al4 V pedicle screws in vitro and in vivo. J Bone Joint Surg Am. 2008;90:2485–98.
70. Ottosson M, Jakobsson A, Johansson F. Accelerated wound closure-differently organized nanofibers affect cell migration and hence the closure of artificial wounds in a cell based in vitro model. PLoS One. 2017;12:e0169419.
71. Ranjbar-Mohammadi M, Bahrami SH. Development of nanofibrous scaffolds containing gum tragacanth/poly (ε-caprolactone) for application as skin scaffolds. Mater Sci Eng C Mater Biol Appl. 2015;48:71–9.
72. Webb K, Hlady V, Tresco PA. Relative importance of surface wettability and charged functional groups on NIH 3T3 fibroblast attachment, spreading, and cytoskeletal organization. J Biomed Mater Res. 1998;41:422–30.
73. Lieberman JR, Friedlaender GE. Bone regeneration and repair: biology and clinical application. Berlin: Springer; 2005.
74. Karageorgiou V, Kaplan D. Porosity of 3D biomaterial scaffolds and osteogenesis. Biomaterials. 2005;26:5474–91.
75. Betz MW, Yeatts AB, Richbourg WJ, Caccamese JF, Coletti DP, Falco EE, et al. Macroporous hydrogels upregulate osteogenic signal expression and promote bone regeneration. Biomacromolecules. 2010;11:1160–8.